Journal of
Materials Chemistry C

ROYAL SOCIETY
OF CHEMISTRY

COMMUNICATION

View Article Online
View Journal | View Issue

Check for updates

Cite this: *J. Mater. Chem. C*, 2026, **14**, 3061

Received 11th January 2026,
Accepted 6th February 2026

DOI: 10.1039/d6tc00086j

rsc.li/materials-c

Non-monotonic plasmonic alignment governed by liquid-crystalline DNA hydrogel networks

Juri Kim,†[a] Soon Mo Park,†[b] Mingeun Kim,[c] Hee Seong Yun,[ad] Jin Suk Myung,[c]
Woo Jin Choi [c] and Dong Ki Yoon *[ad]

Liquid-crystalline ordering in biopolymer networks provides a powerful yet unexplored route for controlling anisotropy in soft materials. Here, we report a DNA–gold nanorod (GNR) hydrogel that exhibits a non-monotonic dependence of strain-induced plasmonic alignment on DNA concentration. The hydrogel is fabricated through a simple thermal annealing process based on DNA denaturation and rehybridization, forming physically crosslinked networks without chemical crosslinkers. Pronounced mechano-responsive color modulation is observed only within a limited concentration regime. When liquid-crystalline (LC) ordering is insufficiently developed, deformation of the matrix is not effectively transferred to the embedded nanorods. Conversely, when DNA packing becomes excessive, the LC phase evolves into densely polydomain textures, in which abundant domain boundaries disrupt long-range strain propagation and suppress nanorod reorientation despite increased bulk stiffness. Rheological measurements, birefringence imaging, and directional FT-IR spectroscopy consistently support this behavior by revealing concentration-dependent differences in network reorganization and deformation continuity. Finally, spatially programmable mechano-optical encryption is demonstrated as a functional example enabled by concentration-controlled DNA-based hydrogels.

Introduction

Since ancient times, metal nanoparticles have attracted scientists and artisans for their remarkable plasmonic optical properties, as exemplified by the Lycurgus cup and medieval stained glass.[1–5] Their surface plasmon resonance (SPR), which originates from collective oscillations of conduction electrons, can be precisely tuned by adjusting particle size, shape, composition, and interparticle distance.[5–10] Among plasmonic nanostructures, gold nanorods (GNRs) are particularly compelling because their transverse and longitudinal SPR modes respond sensitively to the orientation of the nanorods relative to incident light.[8,11–13] This polarization-dependent behavior enables highly responsive tuning of light–matter interactions and has motivated the development of mechanically reconfigurable plasmonic materials.[13–15] Achieving such responsiveness requires a templating matrix that can impose controlled spatial organization and alignment on embedded nanoparticles under deformation.[16–18]

DNA is a promising candidate for this role. Its π–π stacked double helix provides structural rigidity, and programmable Watson–Crick base pairing allows precise control over nanoscale spacing.[11,19–22] Existing approaches often rely on attaching short synthetic oligonucleotides to nanoparticles, although synthesizing oligonucleotides shorter than 50 base pairs requires costly multistep procedures.[20,21] In contrast, bulk natural DNA, which spans hundreds of nanometers, is inexpensive and behaves as a semiflexible rod. Its phase behavior is well described by Onsager theory for hard rods, which predicts the emergence of liquid-crystalline (LC) ordering when:

$$\phi \times \frac{p}{d} \geq \text{constant}(\sim 4), \alpha = l/p(\text{for } \alpha > 1)$$

where ϕ is the volume fraction of the solute, D is the diameter, L is the contour length, and P is the persistence length. For long DNA, with $D \approx 2$ nm, $L \approx 0.34 \times$ (number of bp), and $p \approx 50$ nm, these parameters satisfy the Onsager criterion for the onset of liquid crystalline order. Increasing concentration drives transitions from isotropic to nematic and eventually columnar LC phases.[23–28] Crucially, long DNA chains uniquely enable the formation of physical gel networks through a simple thermal cycling process. Thermal cycling above 90 °C induces partial denaturation, and subsequent cooling generates

---

[a] Department of Chemistry, Korea Advanced Institute of Science and Technology (KAIST), Daejeon 34141, Republic of Korea. E-mail: nandk@kaist.ac.kr
[b] Department of Chemical and Biomolecular Engineering, Cornell University, Ithaca 14853, USA
[c] Digital Chemistry Research Center, Korea Research Institute of Chemical Technology (KRICT), Daejeon 34114, Republic of Korea
[d] GIST InnoCORE AI-Nano Convergence Initiative for Early Detection of Neurodegenerative Diseases, Gwangju Institute of Science and Technology, 61005 Gwangju, Republic of Korea

† J. Kim and S. M. Park contributed equally to this paper.

physical crosslinks through random rehybridization.[29–31] These reversible networks, together with DNA's intrinsic LC behavior, provide a dynamic yet ordered scaffold for organizing anisotropic plasmonic nanostructures. In liquid crystalline elastomers (LCEs), the transition from polydomain to monodomain states has been extensively investigated because it strongly influences bulk elasticity and macroscopic deformation.[32–34] However, how such LC domain structures affect embedded particles in composite systems remains far less understood. The influence of DNA-derived LC polydomains on hydrogel network formation during thermal processing and on the resulting alignment of anisotropic nanoparticles has not been explored.

Here, we demonstrate the fabrication of gold nanorod (GNR)-embedded anisotropic DNA hydrogels using thermal denaturation and rehybridization, and we examine their tunable plasmonic optical properties across a range of DNA concentrations. To identify the optimal concentration range that maximizes mechanical robustness and strain-induced color modulation, we performed polarized light microscopy, polarized FT-IR spectroscopy, and rheological measurements. These measurements reveal that the LC domains play a central role in mediating GNR alignment. At DNA concentrations that support liquid-crystalline ordering without extensive polydomain formation, coherent strain transfer to the nanorods is achieved, resulting in strong alignment. At higher concentrations, the LC phase becomes densely polydomain, and the numerous domain boundaries interrupt deformation pathways and diminish alignment efficiency. This LC-directed mechanical response enables mechano-optical functions such as strain-dependent plasmonic encryption and highlights an unexplored connection between biopolymer LC phase behavior and plasmonic anisotropy in soft materials.

Results and discussions

Fabrication of DNA–GNR hydrogel

The fabrication process and molecular organization of the DNA–GNR hydrogels are illustrated in Fig. 1. Crude salmon DNA was employed as the polymer matrix because it is readily available, inexpensive (approximately \$0.1 per mg from commercial suppliers), and possesses sufficient contour length ($\sim$2000 bp) to form entangled networks at concentrations of tens of mg mL^{-1}. Upon heating to 90 °C, the duplex chains partially denature, and cooling induces random rehybridization among long fragments. Owing to the large contour length and high molecular crowding, the original complementary pairing is rarely restored, resulting in physical crosslinking through transient base pairing and entanglement. With a contour length of $\sim$680 nm and a persistence length of 50 nm, the DNA behaves as a semiflexible polymer capable of forming liquid-crystalline (LC) phases above approximately 40 mg mL^{-1}, providing an anisotropic microenvironment suitable for directing the alignment of embedded gold nanorods (GNRs).[11]

GNRs with 40–50 nm in length were synthesized by a seed-mediated growth method and subsequently rendered compatible with DNA through ligand exchange with methoxypoly(ethylene glycol) thiol (PEG–SH), replacing the cationic surfactant cetyltrimethylammonium bromide (CTAB) and preventing electrostatic aggregation.[11,35–37] PEGylation did not alter the plasmonic spectrum (Fig. S2). PEG–GNRs were mixed with DNA solutions ranging from 25 to 100 mg mL^{-1}, encompassing both isotropic and nematic regimes (Fig. S3). The presence or absence of GNRs appeared to have minimal influence on the formation of the DNA liquid crystalline phase, as birefringence was consistently observed under polarized optical microscopy near $\sim$40 mg mL^{-1}. Samples are referred to as "D*x*", where *x* denotes the DNA concentration in mg mL^{-1}.

To induce gelation, mixtures were injected into glass-sandwich molds (Fig. 1a), heated to 90 °C for 1 h, and cooled to room temperature. Rheological measurements revealed increases in both G' and G'' after thermal cycling, indicating the formation of a physically crosslinked DNA network (Fig. S4).[29,31,38] In all cases, the storage modulus (G') and loss modulus (G'') increased following the thermal cycle, indicating enhanced mechanical strength compared with the original precursor solution. These results support the hypothesis that thermally denatured DNA forms crosslinking points with other denatured single-stranded DNA molecules, thereby leading to gelation.

The effects of DNA concentration on the internal structure of the precursor solutions and the structural changes induced by gelation were examined using linear- and cross-polarized optical microscopy (L-POM and C-POM) (Fig. 1b, c and Fig. S5, S6). In precursor solutions, C-POM images remained dark below 50 mg mL^{-1}, while 50 mg mL^{-1} solution exhibited increased brightness. At concentrations above 75 mg mL^{-1}, well-defined LC domains displaying second-order retardation became evident, consistent with the development of nematic packing.[39] Despite these local domains, L-POM images of all precursor solutions appeared uniformly bluish, suggesting an absence of macroscopic orientation. After gelation, gels originating from concentrations below 50 mg mL^{-1} showed reduced birefringence, becoming nearly dark. Gel formed from 75 mg mL^{-1} solution retained overall brightness although their textures were partially altered, whereas gels above 75 mg mL^{-1} preserved strong birefringence and distinct LC domains. These trends indicate that the gelation process can disrupt alignment at low concentrations, while the higher viscosity at elevated concentrations helps maintain nematic ordering. In this context, the gels exhibit a polydomain morphology, characterized by multiple regions with different local liquid-crystalline orientations, as reflected in spatial variations of optical textures in C-POM images. As shown in Fig. S7, the average domain area decreases sharply above 60 mg mL^{-1}, accompanied by a rapid increase in the number of domains, with particularly pronounced changes observed in the high-concentration regime (85–100 mg mL^{-1}). Although gelation induced subtle modifications in local textures, L-POM colors remained unchanged, consistent with random macroscopic DNA orientation. UV-Vis

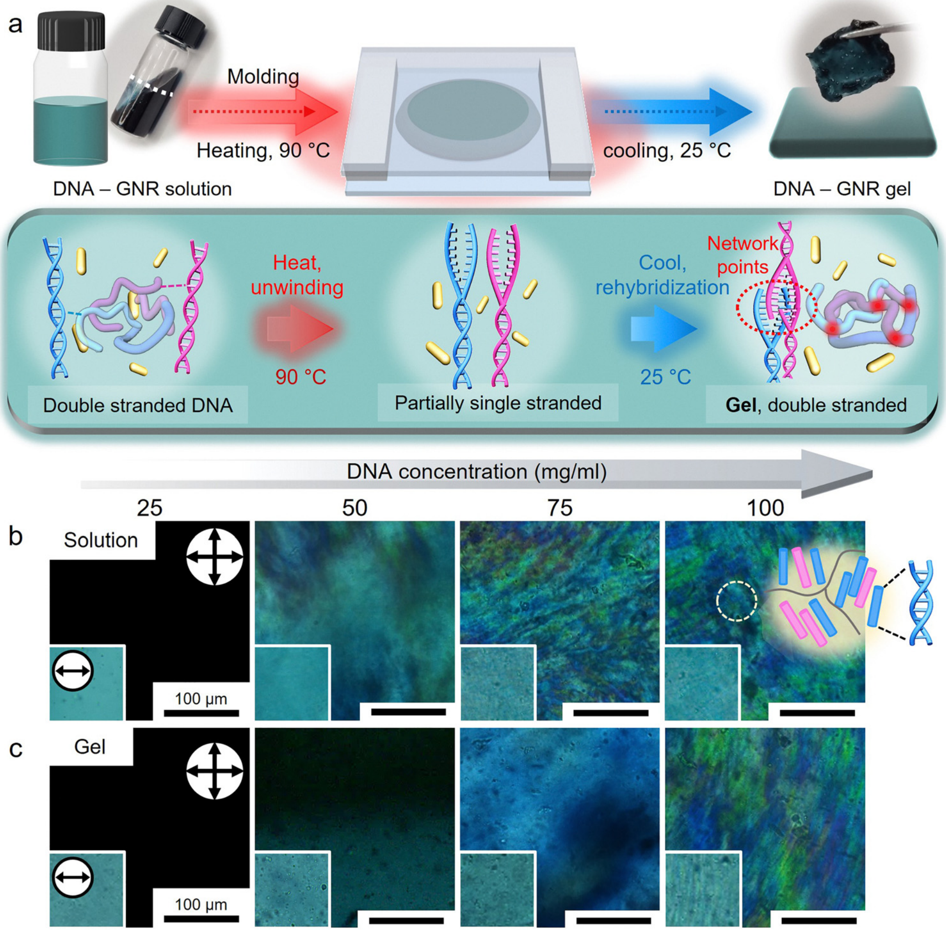

Fig. 1 Fabrication of DNA–gold nanorod (GNR) hydrogel. (a) Schematic illustration of the fabrication process for the DNA–GNR hydrogel. Polarized optical microscopy images of DNA–GNR (b) solutions and (c) gels at varying DNA concentrations. The large images show crossed polarized images(C-POM), and the inset images show linearly polarized images (L-POM). Black arrows indicate the polarization direction. The inset schematically illustrates the director alignment of DNA as the concentration increases. All scale bars represent 100 μm.

spectra further confirmed that the plasmonic peak positions were invariant with respect to DNA concentration (Fig. S8).

Observation of plasmonic color during stretching depending on DNA concentration

It is well established that anisotropic nanoparticles embedded within polymer matrices can align along the direction of applied mechanical strain when the surrounding matrix exhibits sufficient elasticity.[40,41] This alignment arises from shear forces generated during polymer chain reorientation, underscoring the importance of the matrix's viscoelastic properties in dictating nanoparticle orientation. Given that DNA concentration strongly influences the viscoelasticity of the hydrogel, we systematically investigated strain-induced plasmonic color changes in DNA–GNR hydrogels across various DNA concentrations to identify the concentration range that yields the most pronounced optical response (Fig. 2).

Mechanical strain was applied to hydrogels with different DNA concentrations, and the resulting plasmonic color changes were examined as a function of both the incident light's linear polarization state and its orientation relative to the stretching direction (Fig. 2a and b). L-POM images were acquired under various polarization angles (θ), defined as the angle between the polarization direction of light and the stretching direction of the gel. Representative L-POM images recorded just before fracture are shown in Fig. 2b. The hydrogel containing 25 mg mL^{-1} DNA displayed a bluish color that showed negligible change upon stretching, regardless of θ. In contrast, hydrogels containing 50 mg mL^{-1} and 75 mg mL^{-1} DNA exhibited distinct polarization-dependent color changes: at $\theta = 0°$ (parallel), the blue brightness intensified, whereas at $\theta = 90°$ (perpendicular), the color shifted from blue to red. These results indicate that GNRs became aligned along the stretching direction at these concentrations, consistent with the expected polarization dependence of their longitudinal SPR mode.[11] Notably, the gel containing 75 mg mL^{-1} showed more pronounced color contrast than that containing 50 mg mL^{-1}, suggesting that denser DNA packing facilitates more effective strain-induced GNR alignment. SEM images confirmed that the observed chromatic changes indeed originate from GNR

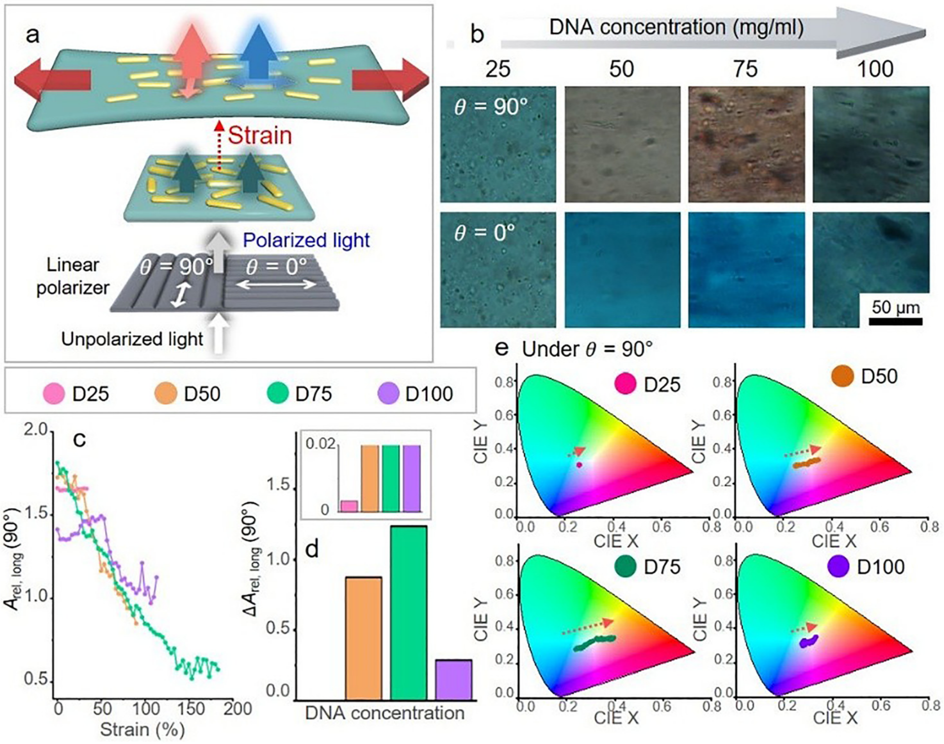

Fig. 2 Plasmonic color changes during stretching as a function of DNA concentration (a) schematic illustration showing the color change in DNA–GNR hydrogels under applied strain. (b) Linear polarized optical microscopy (L-POM) images taken just before fracture under perpendicular (θ = 90°) and parallel (θ = 0°) polarization relative to the stretching direction. Scale bar = 50 μm. (c) Relative longitudinal absorbance, $A_{\mathrm{rel,long}}(90°)$, as a function of strain for different DNA concentrations. (d) Strain-induced optical response quantified as differential absorbance, $\Delta A_{\mathrm{rel,long}}(90°)$, with the inset showing the same data on a lower scale for comparison. (e) CIE color coordinates of hydrogels under strain at θ = 90°, illustrating the direction of plasmonic color shifts (red dashed arrows) with increasing mechanical deformation.

reorientation, as the nanorods were aligned along the direction of applied strain (Fig. S9).

At a higher concentration of 100 mg mL^{-1}, however, the optical response differed. The brightness at θ = 0° was reduced relative to the 75 mg mL^{-1} gel, and at θ = 90°, the gel exhibited a bluish color rather than the red hue observed at intermediate concentrations. These observations suggest that an optimal DNA concentration is required to support chain reorientation under strain, thereby enabling efficient GNR alignment. Additional polarization-dependent optical images over finer concentration intervals and strain levels are provided in Fig. S10–S12.

To quantify GNR alignment during stretching, plasmonic absorbance spectra $A(\lambda,\theta)$ were measured under varying strain, where λ denotes wavelength and θ the polarization angle relative to the stretching direction. Measurements were conducted using a spectrometer equipped with a linear polarizer. In previous work, we demonstrated that the longitudinal SPR absorbance (A_{long}) is maximized when the GNRs are oriented parallel to the polarization direction, whereas the transverse SPR peak (A_{trans}) is maximized when oriented perpendicularly.[11] In the present study, negligible peak wavelength shifts were observed under strain, whereas the absorbance intensities changed significantly. Therefore, our analysis focused on absorbance intensity variations as indicators of strain-induced GNR alignment.

When θ = 90° (perpendicular), the transverse peak $A_{\mathrm{trans}}(90°)$ at 510 nm showed minimal change with strain, whereas the longitudinal peak $A_{\mathrm{long}}(90°)$ at 620 nm progressively decreased (Fig. S13a). Although gel thinning during stretching resulted in an overall decrease in absorbance across the spectrum, the selective decrease of the longitudinal peak clearly indicates GNR alignment along the stretching axis. To normalize intensity changes, the measured absorbance at each wavelength was divided by the maximum transverse peak intensity at θ = 90° ($A_{\mathrm{trans}}(90°)$) (Fig. S12b and S13), yielding the relative absorbance:

$$A_{\mathrm{rel}}(\lambda, 90°) = \frac{A(\lambda, 90°)}{A_{\mathrm{trans}}(90°)}$$

We then tracked the maximum relative longitudinal absorbance, $A_{\mathrm{rel,long}}(90°)$, for hydrogels with varying DNA concentrations (Fig. 2c, Fig. S15a). Absorbance was measured up to the critical strain just before fracture, and differential absorbance was calculated to evaluate the optical response (Fig. 2d, Fig. S15):

$$\Delta A_{\mathrm{rel,long}}(90°) = A^{\mathrm{extension}}_{\mathrm{rel,long}}(90°) - A^{\mathrm{pristine}}_{\mathrm{rel,long}}(90°)$$

Consistent with the qualitative observations in Fig. 2b, the hydrogel containing 25 mg mL^{-1} DNA exhibited negligible alignment ($\Delta A_{\text{rel,long}}(90^\circ)$ = 0.003). Increasing the concentration to 50 and 75 mg mL^{-1} yielded substantial increases in $\Delta A_{\text{rel,long}}(90^\circ)$, reaching 0.875 and 1.240, respectively, indicative of enhanced GNR alignment at these concentrations. These findings suggest that LC domains within the DNA matrix play a critical role in enabling nanoparticle reorientation under strain. As DNA concentration increases, the improved packing density promotes orientational order and reinforces the local environment required for GNR alignment. However, at 100 mg mL^{-1}, $\Delta A_{\text{rel,long}}(90^\circ)$ decreased to 0.288, significantly lower than the value for 75 mg mL^{-1}. This decline suggests that beyond a certain concentration, excessive packing density may hinder the deformation required for effective GNR alignment. A more detailed discussion of this behavior is provided in the next section. A parallel analysis at $\theta = 0^\circ$, where changes in the transverse absorbance are inherently smaller, revealed consistent polarization-dependent trends (Fig. S13b).

To visualize absorbance changes more intuitively, we performed CIE color mapping with $A_{\text{rel}}(\lambda,90^\circ)$ (Fig. 2e; additional data for $\theta = 0^\circ$ are provided in Fig. S16 and S17). Because only the relative intensities of the transverse and longitudinal SPR modes varied, the chromaticity coordinates traced linear trajectories. The magnitude of these trajectories followed the order 75 mg mL^{-1} > 50 mg mL^{-1} > 100 mg mL^{-1} > 25 mg mL^{-1}. Notably, these changes cannot be attributed merely to variations in nanoparticle density or overall gel brightness, as CIE coordinates encode spectral balance rather than absolute intensity. Therefore, the chromaticity shifts directly reflect modulation of the longitudinal-to-transverse SPR ratio and confirm that the observed differences in ΔA_{rel} arise primarily from GNR alignment rather than from concentration-dependent optical artifacts. These results demonstrate that the viscoelastic properties of the DNA matrix, governed by DNA concentration, critically dictate the shear-induced alignment of GNRs and the resulting mechanochromic response.

Mechanistic analysis of DNA alignment and rheological behaviour

The influence of initial DNA concentration on the viscoelasticity of the hydrogel and the strain-induced alignment of embedded GNRs was examined through their polarization-dependent plasmonic responses. Both the magnitude of color modulation and the fracture strain varied strongly with DNA concentration, revealing an optimal composition at which tunability and mechanical robustness are maximized. This behavior suggests that GNR alignment is dictated by the anisotropic mechanical response of the DNA matrix, which becomes pronounced only above the threshold for liquid-crystalline ordering. The concentration-dependent trends observed here motivated a detailed investigation of how LC domain structure and viscoelastic properties together determine alignment efficiency (Fig. 3a), which was probed using C-POM and rheological measurements in the following sections.

To elucidate how DNA concentration influences chain reorganization under strain, the structural response of DNA-only hydrogels to uniaxial deformation was examined using C-POM with a full-wave retardation plate (λ = 530 nm) during stretching (Fig. 3b). In the undeformed state, hydrogels containing 25–75 mg mL^{-1} DNA displayed magenta textures consistent with random chain orientation, whereas the 100 mg mL^{-1} gel exhibited multicolored birefringence arising from densely packed polydomains approaching a columnar LC phase. Under tensile deformation, gels containing 25–75 mg mL^{-1} DNA progressively transitioned toward monodomain alignment. The 25 mg mL^{-1} gel developed blue coloration near $\varepsilon/\varepsilon_{\text{f}} \approx 0.7$, while 50 and 75 mg mL^{-1} gels reached similar alignment at lower $\varepsilon/\varepsilon_{\text{f}} \approx 0.5$, demonstrating enhances nematic ordering, thereby enabling uniaxial alignment of DNA chains at lower $\varepsilon/\varepsilon_{\text{f}}$ values under mechanical stress.[42–45] The 75 mg mL^{-1} sample exhibited higher-order interference colors near fracture, reflecting strong orientational coherence under load.

Birefringence (Δn) was quantified from retardation Γ using the Michel–Levy chart and the relation

$$\Gamma = t \times \Delta n$$

with a nominal thickness of 500 μm (Fig. 3c, Fig. S18a). Higher DNA concentrations produced larger retardation changes once the blue interference region was reached, corresponding to a steeper increase in Δn under strain. Before the onset of blue birefringence, all gels exhibited slow Δn growth characteristic of soft elastic behavior.[32–34] After chain alignment was established, a linear elastic regime ensued, producing rapid birefringence increases due to reduced interchain spacing.[43,46] Assuming isotropic contraction during stretching, the corrected birefringence trends accounting for thickness change are shown in Fig. S17b. Although the absolute birefringence values were larger, the overall trends were consistent with those assuming constant thickness.

Polarization-dependent Fourier-transform infrared (FT-IR) spectroscopy further confirmed this alignment behavior: prior to stretching, no preferential orientation was detected, but under strain the 50 and 75 mg mL^{-1} gels showed clear increases in the 965 cm^{-1} DNA backbone peak when the incident polarization was parallel to the strain axis (Fig. S19).[47,48] Near-complete alignment was recorded for the 75 mg mL^{-1} gel, whereas the 100 mg mL^{-1} gel showed no significant polarization dependence, consistent with its persistent polydomain texture. These results indicate that increasing DNA concentration does not simply enhance elasticity. Instead, the formation of densely packed polydomains at high concentrations suppresses the strain-induced polydomain-to-monodomain transition, thereby limiting effective network reorganization. As a consequence, the viscoelastic response of the gel is strongly affected by how polydomain LC structures interfere with intermolecular crosslink formation within the network.[49–51]

The extent of network formation across DNA concentrations was assessed by analyzing the temperature-dependent ratio of the loss modulus (G'') to the storage modulus (G'), represented as $\tan\delta$ (Fig. 3d). Previous reports have demonstrated that single-stranded DNA (ssDNA) exhibits greater flexibility and

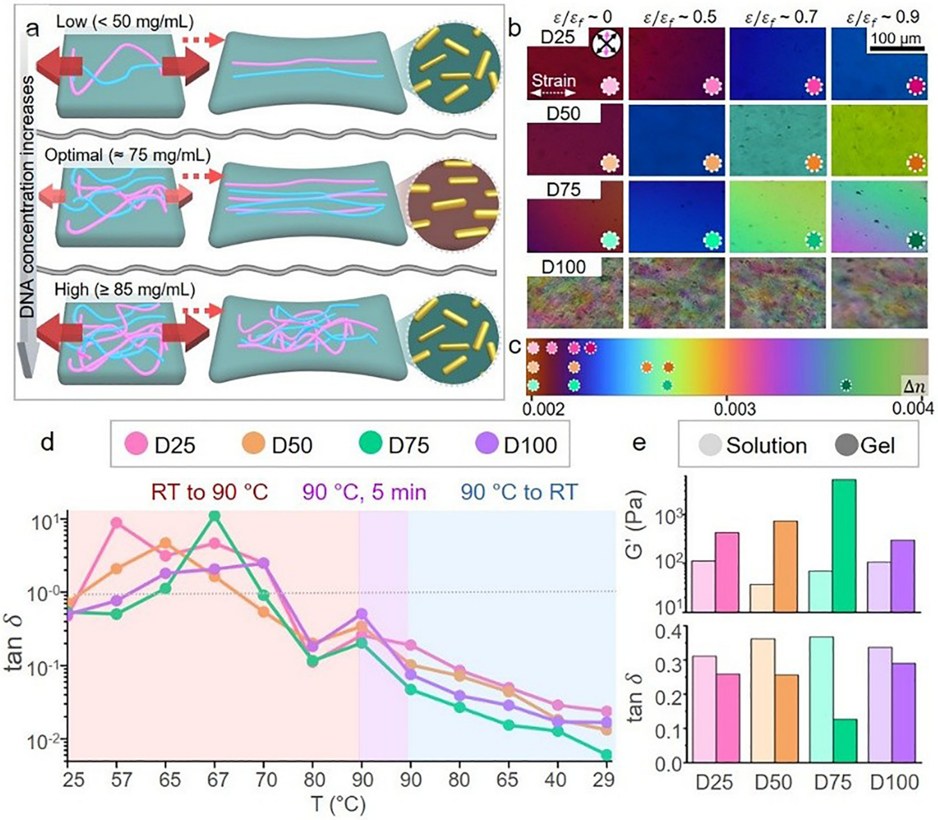

Fig. 3 Mechanistic analysis of DNA alignment and rheological behaviour as a function of DNA concentration. (a) Schematic representation of the internal chain configuration at different DNA concentrations during tensile stretching of the DNA–GNR gel. (b) C-POM image series acquired during the tensile process for each gel composition. (ε_f: fracture strain) pink arrow indicates slow axis of waveplate. All scale bars = 100 μm. (c) Quantitative birefringence maps derived from C-POM images using a Michel–Levy-based color calibration to visualize optical retardance (Δn) (d) rheological measurements showing tan δ as a function of temperature during a full heating–cooling cycle. (e) Comparison of the storage modulus (G') and tan δ values between the solution and gel states, measured at 1% strain and 1 rad s^{-1}.

typically higher G'' than double-stranded DNA (dsDNA) at equivalent concentrations, leading to distinguishable viscoelastic transitions in DNA-based networks.[52–56] Accordingly, a sharp increase in tan δ upon heating was interpreted as the unwinding phase of DNA strands, while a subsequent decrease upon cooling reflected the rehybridization of ssDNA into dsDNA. To assess these characteristics, DNA–GNR solutions were subjected to a thermal cycle consisting of heating from 25 °C to 90 °C, holding at 90 °C for 5 minutes, and then cooling to room temperature. Upon heating to 90 °C, tan δ increased due to strand unwinding, with peak values reflecting maximum molecular mobility. The highest peak occurred at 75 mg mL^{-1} and the lowest at 100 mg mL^{-1}, indicating that excessive packing and the development of polydomain LC structures restrict strand separation during thermal activation (tan δ: 75 mg mL^{-1} > 25 mg mL^{-1} > 50 mg mL^{-1} > 100 mg mL^{-1}) (Fig. S20a). During cooling, tan δ decreased as rehybridization progressed, yielding final values in the order 75 < 50 < 100 < 25 mg mL^{-1}. These results indicate that renaturation and network reconstruction are most effective at 75 mg mL^{-1}, while both low and excessively high concentrations limit crosslink formation. The difference between the peak and final tan δ (Δtan δ) was used as an indicator of the extent of network reorganization and effective crosslink formation during the thermal cycle. This value was greatest for the 75 mg mL^{-1} sample and smallest for the 100 mg mL^{-1} sample (Fig. S20b), indicating that strand unwinding and subsequent rehybridization were most extensive at the intermediate concentration. In contrast, the minimal Δtan δ observed at 100 mg mL^{-1} suggests restricted hydrogen-bond disruption and inefficient network formation, likely due to severe molecular crowding. Notably, both the peak tan δ and Δtan δ exhibited similar concentration-dependent trends (Fig. S20a and b), implying that most of the thermally unwound ssDNA contributes to crosslink formation only within an optimal concentration range.

Comparison of viscoelastic properties before and after gelation further supported this interpretation, based on measurements of the storage modulus (G') and tan δ at room temperature for both the solution and gel states across all DNA concentrations (Fig. 3e, Fig. S20c and d). In the solution state, G' values ranged from 40 to 110 Pa without clear concentration dependence, indicating that increasing DNA concentration alone does not substantially alter the initial elastic response of the precursor solutions. Following gelation, G' increased for all samples, but both the absolute change ($\Delta G' = G'(\text{gel}) - G'(\text{solution})$) and the fold change varied markedly with concentration. At 75 mg mL^{-1}, G' increased from $\sim$70 Pa to 5120 Pa, corresponding to $\Delta G' \approx 5050$ Pa and an approximately 74-fold enhancement, the largest among all samples. In contrast, gels formed at 25 and 50 mg mL^{-1} exhibited moderate increases, with $\Delta G'$ values of $\sim$310 Pa and $\sim$700 Pa (about 10-fold and 13-fold, respectively). The 100 mg mL^{-1} sample showed only a minor increase to $\sim$300 Pa, yielding the smallest $\Delta G'$ ($\sim$190 Pa) and a fold change of $\sim$2.7.

Tan δ exhibited analogous concentration-dependent behavior. In the solution state, tan δ remained near $\sim$0.3 for all gels. After gelation, tan δ decreased to 0.25 for 25 and 50 mg mL^{-1} decreased further to 0.12 for 75 mg mL^{-1}, and remained relatively high at 0.29 for 100 mg mL^{-1}. Consistent with these trends, the largest Δtan δ, defined as the difference between tan δ in the solution and gel states, was observed at 75 mg mL^{-1} (0.24), whereas the smallest occurred at 100 mg mL^{-1} (0.04). Collectively, the pronounced increases in G' and reductions in tan δ at 75 mg mL^{-1} indicate the most efficient structural reorganization and highest effective crosslinking density during gelation, while the minimal changes at 100 mg mL^{-1} suggest limited network formation.

Taken together, these observations demonstrate that the nonlinear dependence of gel elasticity on DNA concentration is governed by the emergence of liquid-crystalline polydomain structures and their impact on physical crosslink formation. DNA hybridization is inherently cooperative, and increasing concentration generally enhances duplex stability, as reflected by an elevated melting temperature (T_m) associated with more efficient rehybridization.[57–59] However, once densely packed LC polydomains develop at high concentration, the resulting domain boundaries impose structural constraints that restrict strand mobility, suppress thermal unwinding and rehybridization during gelation, and interrupt deformation pathways. Under these conditions, severe reductions in configurational entropy and molecular crowding further exacerbate the inhibition of effective network formation.[59,60] As a result, network connectivity remains insufficient at high concentration (100 mg mL^{-1}), allowing LC polydomain textures to persist after gelation (Fig. 1b and c), analogous to behaviors reported in liquid crystalline elastomer systems with inadequate crosslink density.[34,61,62]

Consequently, the strain-induced alignment of GNRs is dictated by the mechanical evolution of the DNA matrix rather than DNA concentration alone. Hydrogels containing 50–75 mg mL^{-1} DNA avoid extensive polydomain formation while maintaining sufficient LC order, thereby achieving an optimal balance between cooperative chain reorientation and effective crosslink formation. The 50 mg mL^{-1} sample exhibits moderate birefringence and limited plasmonic anisotropy due to incomplete LC development, whereas the 75 mg mL^{-1} sample displays pronounced uniaxial ordering and the strongest polarization-dependent plasmonic modulation.[41,63] In contrast, at 100 mg mL^{-1}, persistent LC polydomains inhibit coherent deformation and suppress network reorganization, preventing monodomain alignment of DNA chains and resulting in negligible GNR reorientation under strain. These results establish a clear non-monotonic relationship between DNA concentration and alignment capacity, in which increasing concentration enhances ordering and strain transfer only up to an optimal threshold, beyond which polydomain persistence and entropic constraints dominate the mechanical response.

Demonstration of multifunctional DNA–GNR hydrogels

In addition to the intrinsic hygroscopicity and physiologically relevant mechanical properties typical of hydrogels, the DNA–GNR hydrogels developed in this study exhibit a range of multifunctional characteristics. These functionalities arise from their biocompatible composition, consisting exclusively of salmon DNA and gold nanorods, together with their straightforward fabrication *via* thermal processing.

One notable feature is the formation of a physically crosslinked network through chain entanglement and hydrogen bonding between complementary DNA base pairs. Owing to the highly hygroscopic nature of DNA, the resulting hydrogels undergo rapid aqueous degradation. When immersed in water, the DNA–GNR hydrogels completely disintegrated within 12 h, highlighting their environmentally benign and transient character (Fig. 4a).

Because gelation relies solely on thermal denaturation and subsequent rehybridization of DNA strands, localized heating can be employed to selectively induce gel formation. By applying heat using a heating block at the interface between gels with and without embedded GNRs, localized gelation was triggered, enabling effective interfacial healing between the two regions (Fig. 4b).

The precursor DNA–GNR solutions also exhibit a viscoelastic profile that is neither excessively fluidic nor overly rigid, allowing facile shaping into diverse geometries. Exploiting this moldability, hydrogels were fabricated in the shape of the letter "K" by casting the solution into a mold between glass substrates, and thread-like structures were produced using a capillary tube. These geometrically defined hydrogels retained their plasmonic optical properties and displayed polarization-dependent color responses, confirming that their optical functionality is preserved across different forms (Fig. 4c).

In addition, the tunable plasmonic properties of GNRs were leveraged to further diversify the optical response of the hydrogels under mechanical deformation. By varying the concentration of ascorbic acid during seed-mediated growth, GNRs with different aspect ratios (40 × 17 nm, 47 × 15 nm, and 50 × 10 nm) were synthesized and characterized by scanning electron microscopy (SEM) and UV-vis spectroscopy. When incorporated into DNA–GNR hydrogels and subjected to uniaxial strain, each formulation exhibited a distinct plasmonic color response that depended on the polarization state of the incident light (Fig. 4d).

Collectively, these results demonstrate that, despite being composed solely of DNA and GNRs and fabricated through a simple thermal cycle, the resulting hydrogels integrate biodegradability, healability, moldability, and polarization-tunable plasmonic functionality. This combination of properties establishes DNA–GNR hydrogels as a versatile platform for optical and stimuli-responsive soft-material applications.

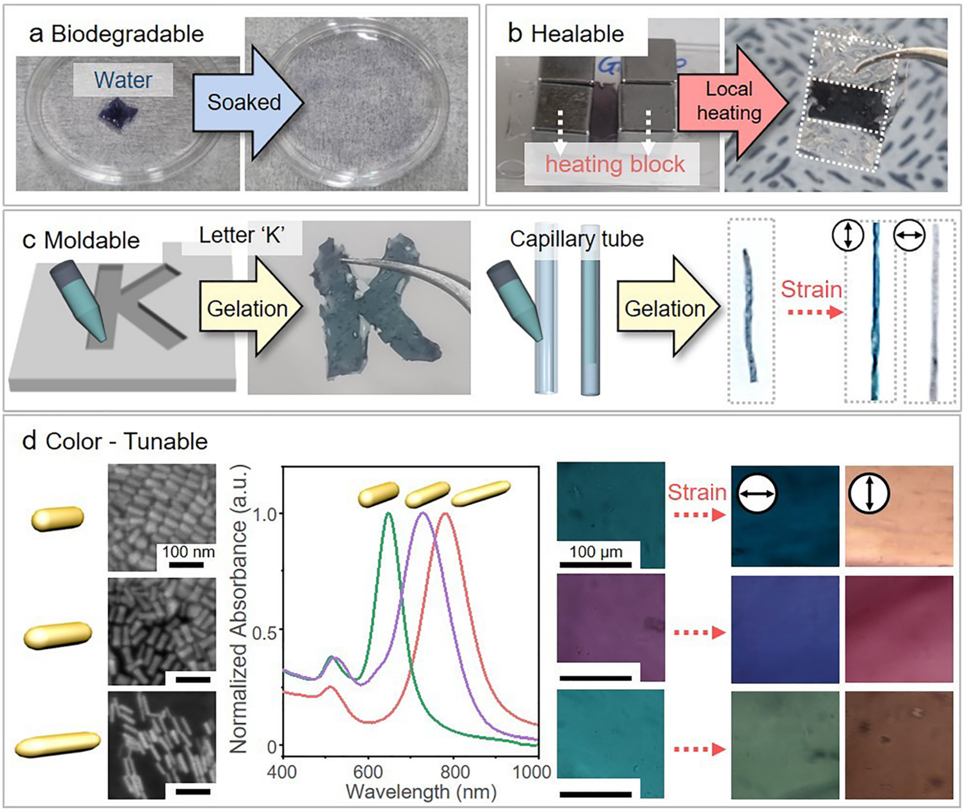

Fig. 4 Demonstration of the multifunctional hydrogel. (a) Biodegradable, (b) healable, (c) moldable, and (d) color-tunable properties of the DNA–GNR hydrogel.

Plasmonic color patterning *via* spatial control of DNA concentration

To clarify the role of DNA matrix concentration in governing the alignment behavior of embedded GNRs, it was found that modulation of DNA concentration alone determines whether the hydrogel can support strain-induced GNR reorganization and thus exhibit anisotropic optical functionality. DNA–GNR hydrogels with matrix concentrations between 50 and 75 mg mL^{-1} supported effective nanorod alignment under mechanical strain, as evidenced by pronounced plasmonic color shifts and increased absorbance anisotropy (ΔA_{rel}) under polarized illumination (Fig. 2 and 3). In contrast, hydrogels with concentrations outside this range failed to induce GNR alignment, resulting in negligible optical response.

Building on this concentration-dependent behavior, a mechanoresponsive optical encryption platform was developed in which spatial encoding is achieved solely through local modulation of DNA concentration (Fig. 5). The fabrication procedure is schematically illustrated in Fig. 5a. Two DNA–GNR precursor solutions were prepared: one at 75 mg mL^{-1}, corresponding to the optimal concentration for strain-induced GNR alignment, and one at 100 mg mL^{-1}, which exhibits limited chain mobility due to suppressed crosslinking efficiency and a weak mechanical response. These concentrations were selected based on rheological metrics ($\Delta G'$, $\Delta \tan\delta$; Fig. 3e and Fig. S20) and optical anisotropy analysis (ΔA_{rel}; Fig. S14), which show maximal response at 75 mg mL^{-1} and minimal response at 100 mg mL^{-1}. Using the inherent moldability of the DNA–GNR precursor, a letter "K" was first cast from the 75 mg mL^{-1} formulation. After gelation, the surrounding region was filled with the 100 mg mL^{-1} solution, and localized heating at the interface promoted physical crosslinking through hydrogen-bond rehybridization, seamlessly integrating the two regions into a single hydrogel. Upon application of tensile strain and observation under polarized light, the "K" region underwent strain-induced GNR alignment, producing a distinct reddish color shift, while the surrounding matrix remained optically inactive due to the absence of nanorod reorientation (Fig. 5b).

The robustness of this concentration-based encryption strategy was validated using three different patterned geometries: (i) a half–half configuration, (ii) a circular pattern, and (iii) a "K"-shaped pattern (Fig. 5c). In the undeformed state, no visible contrast was observed, reflecting the identical appearance of the 75 mg mL^{-1} and 100 mg mL^{-1} regions in the absence of strain. Upon application of moderate strain ($\varepsilon \approx 40\%$), weak polarization-dependent contrast emerged selectively in the lower-concentration regions. With increasing strain, a pronounced reddish color developed exclusively in the 75 mg mL^{-1} domains, effectively revealing the encoded patterns under polarized illumination.

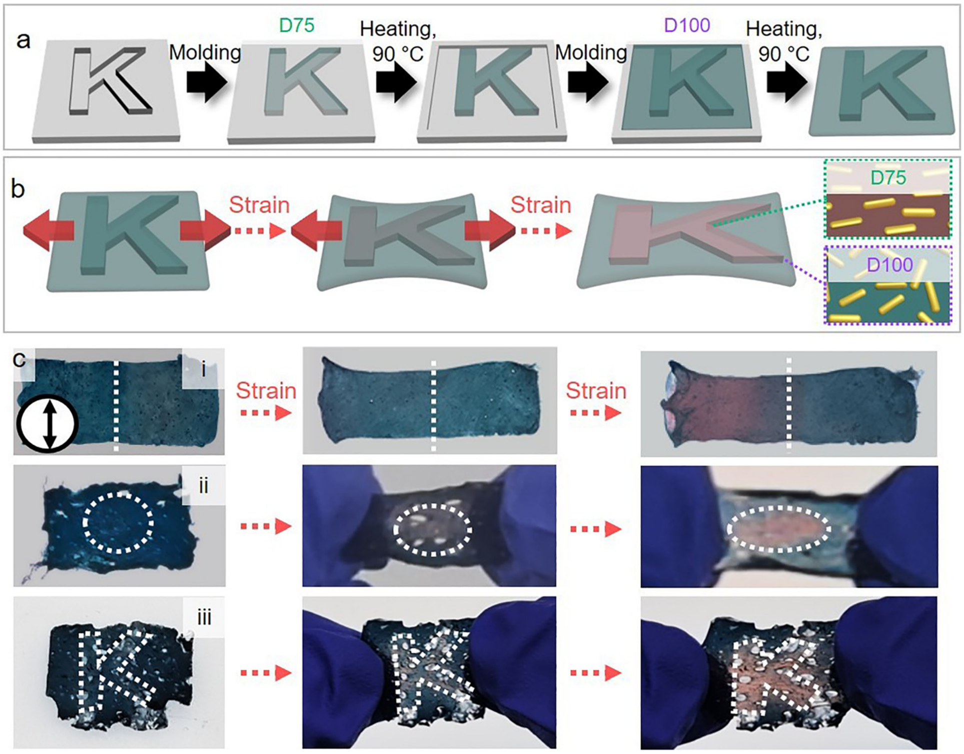

Fig. 5 Demonstration of mechanoresponsive encryption based on spatial DNA concentration patterning. Schematic illustration of (a) the fabrication process and (b) the underlying mechanism. (c) Photographic images before (left) and after stretching (middle and right) for three spatial patterns: (i) half-half, (ii) circular, and (iii) letter 'K', showing that initially hidden patterns become optically visible upon mechanical deformation.

Collectively, these results demonstrate that mechanoresponsive plasmonic encryption can be realized using fully biodegradable and biocompatible materials through a simple fabrication strategy. Notably, the encoding mechanism relies solely on spatial modulation of native DNA concentration within the matrix, without requiring external dyes, complex lithographic processes, or multilayer architectures.

Conclusions

In this work, a polarization-dependent, mechanically responsive DNA–gold nanorod (GNR) hydrogel was demonstrated using a simple and environmentally benign thermal processing route. Partial thermal denaturation of double-stranded DNA during heating, followed by stochastic rehybridization upon cooling, enabled the formation of physically crosslinked and biocompatible hydrogel networks without chemical crosslinkers. When subjected to mechanical deformation, these DNA–GNR hydrogels exhibited strain-induced plasmonic color modulation arising from the alignment of embedded nanorods.

A key finding of this study is that nanorod alignment and the associated optical response depend nonlinearly on DNA concentration. When liquid-crystalline ordering develops without extensive polydomain formation, the DNA network supports efficient crosslinking during gelation and undergoes coherent mechanical deformation under applied strain, enabling effective GNR alignment. In contrast, at higher DNA concentrations, the formation of densely packed liquid-crystalline polydomains restricts strand mobility during thermal processing, suppresses crosslink formation, and disrupts deformation pathways. As a result, the DNA matrix cannot reorganize into a monodomain state under strain, preventing efficient nanorod alignment despite increased polymer content. These results demonstrate that liquid-crystalline polydomain formation, rather than DNA concentration alone, governs the upper limit of mechanical and optical tunability in DNA-based plasmonic hydrogels. It should be emphasized that the quantitative concentration range and alignment behavior reported here are specific to the DNA hydrogel system studied in this work, which is based on salmon sperm DNA and a limited experimental parameter.

Nevertheless, similar non-monotonic viscosity and alignment behaviors have been reported in other liquid crystalline systems, such as graphene oxide dispersions and liquid crystal materials, where internal structural reorganization and phase heterogeneity strongly influence macroscopic mechanical and rheological responses. Based on this perspective, our results suggest that an optimal balance between network connectivity and internal structural heterogeneity is a general design principle for achieving efficient alignment in soft materials.

Beyond elucidating this mechanism, the multifunctional nature of the DNA–GNR hydrogels was demonstrated through applications including biodegradable and healable constructs, shape-moldable architectures, and mechanoresponsive plasmonic encryption achieved *via* spatial control of DNA concentration. Collectively, this study highlights how intrinsic liquid-crystalline behavior of native biomolecules can be harnessed to program anisotropic mechanical and optical responses in soft materials, offering a versatile strategy for designing functional plasmonic systems without relying on complex synthetic DNA modifications.

Experimental

Materials

Double-stranded salmon DNA (deoxyribonucleic acid sodium salt from salmon testes, Sigma-Aldrich) with a Gaussian length distribution centred at ≈2000 bp, corresponding to a molecular weight of 1.3 × 106 g mol^{-1}, was used in this work. Hexadecyltrimethylammonium bromide (CTAB, ≥98%), Gold(III) chloride trihydrate ($HAuCl_4 \cdot 3H_2O$, ≥99.9%), silver nitrate ($AgNO_3$, ≥99%), L-ascorbic acid (≥99%), and methoxy-terminated poly(ethylene glycol) thiol (mPEG-SH, average $M_n \approx 6000$) were purchased from Sigma-Aldrich. Sodium borohydride ($NaBH_4$, ≥98%) was obtained from TCI. All reagents were used without further purification.

Synthesis of gold nanorods. Gold nanorods (GNRs) were prepared by the seed-mediated growth protocol. Briefly, seed particles were generated by reducing $HAuCl_4$ (0.01 M) with ice-cold $NaBH_4$ (0.01 M) in a CTAB (0.10 M) solution under vigorous stirring. The growth solution contained CTAB (0.10 M), $HAuCl_4$ (0.01 M), $AgNO_3$ (0.01 M), and ascorbic acid (0.1 M). After adding freshly prepared seed dispersion to growth solution, the mixture was kept undisturbed for 12 h at 30 °C, yielding nanorods with an average length of 40–50 nm. For ligand exchange, the as synthesized GNR dispersion was centrifuged twice at 10 000 rpm for 15 min to remove excess CTAB, redispersed in 500 μL water, and mixed with 300 μL of 2 mM mPEG-SH. The suspension was gently shaken overnight (≈12 h) and centrifuged again to eliminate unbound PEG. PEGylated GNRs (PEG–GNRs) were stored at 4 °C and used within two weeks to avoid oxidative degradation.

Fabrication of DNA–GNR hydrogel. Salmon DNA was dissolved in water to give 2.5–10 wt% solutions. PEG–GNRs were added to each DNA solution to a final nanoparticle content of 1.3 wt% (identical for all samples) and mixed thoroughly. After degassing (10 000 rpm, 15 min), 400 μL of the mixture was injected between two glass slides separated by a 500 μm silicone spacer (3 cm × 1 cm cavity). Samples were heated at 90 °C on a calibrated hot plate to induce partial DNA denaturation and then allowed to cool passively to room temperature, producing DNA–GNR hydrogels.

General characterization. Birefringence and polarization-dependent plasmonic color of DNA–GNR solutions and gels were examined with a polarized optical microscope (Nikon LV100POL) equipped with a first-order retardation plate (λ = 530 nm) and a DS-Ri1 CCD camera. Scanning electron microscopy (SEM; Hitachi SU8230) was employed to observe the internal structure of hydrogels after the critical point dried using a critical point drier (CPD; Leica EM CPD300).

Rheological measurements. All rheological analyses were carried out on an ARES-G2 (TA Instruments) equipped with 25 mm parallel plate. The advanced Peltier system accessory served as a bottom plate to accurately adjust the temperature by bottom-heating or air/coolant-circulating. For temperature ramps, precursor solutions were loaded at 25 °C, heated to 90 °C at 10 °C min^{-1}, held for 5 min, and cooled back to 25 °C at 3 °C min^{-1}; oscillatory tests were performed at 1 rad s^{-1} and 0.1% strain. For frequency sweeps (1–100 rad s^{-1}, 0.1% strain, 25 °C), disk-shaped hydrogels (25 mm diameter) were prepared. Storage modulus (G'), loss modulus (G'')' and $\tan\delta$ were obtained for each experiment.

FT-IR spectroscopy. Fourier-transform infrared Spectroscopy (Nicolet iS50, Thermo Fischer Scientific Instrument) was employed in the ATR-IR range (400–4000 cm^{-1}). Dried gels, pre-stretched to the desired strain were placed. DNA chain orientation was evaluated by monitoring the intensity of the deoxyribose C–C stretch at 965 cm^{-1} while rotating the incident polarizer in 15° increments.

Author contributions

J. K., S. M. P., and D. K. Y. conceptualized the research project and wrote the manuscript; J. K. prepared the materials, performed optical and mechanical characterizations, and drafted the initial version; S. M. P. analyzed the formation mechanism and refined the manuscript for clarity and coherence; M. K., J. S. M., and W. J. C. contributed to the rheological analysis; H. S. Y. assisted with the correlation between optical images and birefringence data; D. K. Y. supervised the overall research; All authors reviewed and approved the final version of the manuscript.

Conflicts of interest

There are no conflicts to declare.

Data availability

All data relevant for our paper are either provided in the supplementary information (SI) or are available from the authors on request. Supplementary information: SEM images of gold nanorods (GNRs) with varying aspect ratios (S1); UV-Vis-NIR absorption spectra of gold nanorods functionalized with cetrimonium bromide (CTAB) and thiolated polyethylene glycol (PEG–SH) (S2); Schematic illustration of the liquid crystal phases of salmon DNA (S3); Frequency sweep data of DNA–GNR solutions and gels (S4); Polarized optical microscopy images of DNA–GNR solutions at varying DNA concentrations (S5); Polarized optical microscopy images of as-prepared DNA–GNR hydrogels at more finely divided DNA concentrations (S6); Polarized optical microscopy (POM) images of DNA gels acquired over an area of 1.4 × 10^5 μm^2 were analyzed to quantify domain statistics at different DNA concentrations (S7); UV-Vis absorption spectra of as-prepared DNA–GNR hydrogels at various DNA concentrations (S8); SEM images showing the internal microstructure of DNA–GNR hydrogels (S9);

Polarization-dependent optical images of DNA–GNR hydrogels under strain just before fracture (S10); Polarization-dependent optical images of DNA–GNR hydrogels at various DNA concentrations and strain levels, acquired with the polarization direction oriented perpendicular to the stretching direction (S11); Polarization-dependent optical images of DNA–GNR hydrogels at a strain level just before fracture, acquired with the polarization direction oriented parallel to the stretching direction (S12); Polarized absorbance spectra $A(\lambda, 90^\circ)$ of 75 mg mL^{-1} DNA–GNR hydrogels measured as a function of applied strain with polarization perpendicular to the strain axis, and the corresponding relative absorbance spectra $A_{\mathrm{rel}}(\lambda, 90^\circ)$ (S13); Comparison of strain-dependent relative absorbance spectra $A_{\mathrm{rel}}(\lambda, 90^\circ)$ for DNA–GNR hydrogels at varying DNA concentrations (S14); Strain-dependent absorbance changes of DNA–GNR hydrogels under different polarization states and DNA concentrations (S15); CIE color coordinates of DNA–GNR hydrogels with varying DNA concentrations, measured under polarization perpendicular to the stretching direction ($\theta = 90^\circ$) (S16); CIE color coordinates of DNA–GNR hydrogels with varying DNA concentrations, measured under polarization parallel to the stretching direction ($\theta = 0^\circ$) (S17); Quantitative birefringence analysis of DNA hydrogels under uniaxial strain, based on chromatic shift comparison with the Michel–Levy chart (S18); Polar plots of normalized absorbance obtained from polarized FT-IR measurements of DNA–GNR hydrogels at various DNA concentrations and strain levels (S19); Rheological property differences between solution and gel states (S20). See DOI: https://doi.org/10.1039/d6tc00086j.

Acknowledgements

This work was supported by a grant from the National Research Foundation in Korea (RS-2023-00273025 and RS-2024-00411265) and was also funded by the InnoCORE program of the Ministry of Science and ICT (GIST InnoCORE KH0830).

Notes and references

1 U. Kreibig and M. Vollmer, *Optical Properties of Metal Clusters*, Springer US, 1998.
2 S. W. Hsu, A. L. Rodarte, M. Som, G. Arya and A. R. Tao, *Chem. Rev.*, 2018, **118**, 3100–3120.
3 S. Kasani, K. Curtin and N. Wu, *Nanophotonics*, 2019, **8**, 2065–2089.
4 I. Pastoriza-Santos, C. Kinnear, J. Pérez-Juste, P. Mulvaney and L. M. Liz-Marzán, *Nat. Rev. Mater.*, 2018, **3**, 375–391.
5 J. A. Fan, C. Wu, K. Bao, J. Bao, R. Bardhan, N. J. Halas, V. N. Manoharan, P. Nordlander, G. Shvets and F. Capasso, *Science*, 2010, **328**, 1135–1138.
6 A. Gole and C. J. Murphy, *Chem. Mater.*, 2004, **16**, 3633–3640.
7 B. Auguié and W. L. Barnes, *Phys. Rev. Lett.*, 2008, **101**, 143902.
8 H. Chen, L. Shao, Q. Li and J. Wang, *Chem. Soc. Rev.*, 2013, **42**, 2679–2724.
9 S. Yoon, *Bull. Korean Chem. Soc.*, 2024, **45**, 689–698.
10 D. Y. Hyeong and H. Lee, *J. Inf. Disp.*, 2025, **26**, 437–445.
11 Y. J. Cha, D. S. Kim and D. K. Yoon, *Adv. Funct. Mater.*, 2017, **27**, 1703790.
12 J. Pyeon, S. M. Park, J. Kim, J. H. Kim, Y. J. Yoon, D. K. Yoon and H. Kim, *Nat. Commun.*, 2023, **14**, 8096.
13 X. Huang, S. Neretina and M. A. El-Sayed, *Adv. Mater.*, 2009, **21**, 4880–4910.
14 G. Zhao, Y. Zhou, J. Wang, Z. Wu, H. Wang and H. Chen, *Adv. Mater.*, 2019, **31**, 1900363.
15 J. Y. Jung, M. J. Shin, B. Kim, U. J. Pyo, J. G. Son, D. K. Yoon and S. W. Han, *Adv. Opt. Mater.*, 2024, **12**, 2400760.
16 C. J. Murphy and C. J. Orendorff, *Adv. Mater.*, 2005, **17**, 2173–2177.
17 R. C. Ferrier, J. Koski, R. A. Riggleman and R. J. Composto, *Macromolecules*, 2016, **49**, 1002–1015.
18 J. Pérez-Juste, I. Pastoriza-Santos, L. M. Liz-Marzán and P. Mulvaney, *Coord. Chem. Rev.*, 2005, **249**, 1870–1901.
19 Y. J. Cha, S. M. Park, R. You, H. Kim and D. K. Yoon, *Nat. Commun.*, 2019, **10**, 2512.
20 C. Wang, X. Liu, V. Wulf, M. Vázquez-González, M. Fadeev and I. Willner, *ACS Nano*, 2019, **13**, 3424–3433.
21 J. Ryssy, A. J. Lehtonen, J. Loo, M.-K. Nguyen, J. Seitsonen, Y. Huang, B. N. Narasimhan, J. Pokki, A. Kuzyk and S. Manuguri, *Adv. Funct. Mater.*, 2022, **32**, 2201249.
22 W. H. Jung, J. H. Park, S. Kim, C. Cui and D. J. Ahn, *Nat. Commun.*, 2022, **13**, 6193.
23 L. Onsager, *Ann. N. Y. Acad. Sci.*, 1949, **51**, 627–659.
24 M. Nakata, G. Zanchetta, B. D. Chapman, C. D. Jones, J. O. Cross, R. Pindak, T. Bellini and N. A. Clark, *Science*, 2007, **318**, 1276–1279.
25 S. M. Park and D. K. Yoon, *Mater. Horiz.*, 2024, **11**, 1843–1866.
26 B. Kim, G. Park, G. Lee, J. Kim, C. Lee, J. G. Park, M. Kim, J. S. Myung, H. Ahn, S. M. Park, W. J. Choi and D. K. Yoon, *Small*, 2025, **21**, 2500607.
27 J. Kim, Y. S. Choi, G. Park, M. Kim, J. S. Myung, W. J. Choi, S. M. Park and D. K. Yoon, *ACS Nano*, 2023, **17**, 22778–22787.
28 J. Kim, H. Yeon, H. R. Choi, S. M. Park, C. H. Huh, K. C. Choi and D. K. Yoon, *Adv. Opt. Mater.*, 2024, **12**, 2400702.
29 F. Topuz and O. Okay, *Biomacromolecules*, 2009, **10**, 2652–2661.
30 P. Karacan, H. Cakmak and O. Okay, *J. Appl. Polym. Sci.*, 2013, **128**, 3330–3337.
31 S. Basu, S. Pacelli, Y. Feng, Q. Lu, J. Wang and A. Paul, *ACS Nano*, 2018, **12**, 9866–9880.
32 M. Warner, P. Bladon and E. M. Terentjev, *J. Phys. II*, 1994, **4**, 93–102.
33 T. H. Ware, J. S. Biggins, A. F. Shick, M. Warner and T. J. White, *Nat. Commun.*, 2016, **7**, 10781.
34 S. V. Fridrikh and E. M. Terentjev, *Phys. Rev. E:Stat. Phys., Plasmas, Fluids, Relat. Interdiscip. Top.*, 1999, **60**, 1847–1857.
35 G. Von Maltzahn, A. Centrone, J. H. Park, R. Ramanathan, M. J. Sailor, T. Alan Hatton and S. N. Bhatia, *Adv. Mater.*, 2009, **21**, 3175–3180.

36 Q. Liu, M. G. Campbell, J. S. Evans and I. I. Smalyukh, *Adv. Mater.*, 2014, **26**, 7178–7184.

37 U. Erigi, U. Dhumal and M. Tripathy, *J. Chem. Phys.*, 2021, **154**, 124903.

38 X. Wang, H. J. Lim and A. Son, *Environ. Health Toxicol.*, 2014, **29**, e2014007.

39 D. S. Kim, S. Čopar, U. Tkalec and D. K. Yoon, *Sci. Adv.*, 2018, **4**, eaau8064.

40 D. Z. Gunes, R. Scirocco, J. Mewis and J. Vermant, *J. Non-Newtonian Fluid Mech.*, 2008, **155**, 39–50.

41 V. Calabrese, S. Varchanis, S. J. Haward and A. Q. Shen, *Macromolecules*, 2022, **55**, 5610–5620.

42 R. Zentel, *Adv. Mater.*, 1989, **1**, 321–329.

43 J. Schätzle, W. Kaufhold and H. Finkelmann, *Makromol. Chem.*, 1991, **192**, 1235–1236.

44 G. R. Mitchell, W. Guo and F. J. Davis, *Polymer*, 1992, **33**, 68–74.

45 F. J. Davis and G. R. Mitchell, *Polymer*, 1996, **37**, 1345–1351.

46 A. K. Oultache, X. Kong, C. Pellerin, J. Brisson, M. Pézolet and R. E. Prud'homme, *Polymer*, 2001, **42**, 9051–9058.

47 R. Marty, C. N. N'soukpoé-Kossi, D. Charbonneau, C. M. Weinert, L. Kreplak and H. A. Tajmir-Riahi, *Nucleic Acids Res.*, 2009, **37**, 849–857.

48 F. Ma, Y. Ma, C. Du, X. Yang and R. Shen, *J. Mol. Struct.*, 2015, **1100**, 154–161.

49 I. Kundler and H. Finkelmann, *Macromol. Chem. Phys.*, 1998, **199**, 677–686.

50 Z. L. Wu, D. Sawada, T. Kurokawa, A. Kakugo, W. Yang, H. Furukawa and J. P. Gong, *Macromolecules*, 2011, **44**, 3542–3547.

51 D. Ye, Q. Cheng, Q. Zhang, Y. Wang, C. Chang, L. Li, H. Peng and L. Zhang, *ACS Appl. Mater. Interfaces*, 2017, **9**, 43154–43162.

52 S. A. Rice and P. Doty, *J. Am. Chem. Soc.*, 1957, **79**, 3937–3947.

53 J. M. Sturtevant and E. P. Geiduschek, *J. Am. Chem. Soc.*, 1958, **80**, 2911.

54 P. Doty, J. Marmur, J. Eigner and C. Schildkraut, *Proc. Natl. Acad. Sci. U. S. A.*, 1960, **46**, 461–476.

55 J. Marmur and P. Doty, *J. Mol. Biol.*, 1961, **3**, 585–594.

56 E. P. Geiduschek, *J. Mol. Biol.*, 1962, **4**, 467–487.

57 M. Sartor, J. Schwanekamp, D. Halbleib, I. Mohamed, S. Karyala, M. Medvedovic and C. R. Tomlinson, *Biotechniques*, 2004, **36**, 790–796.

58 A. Jayaraman, C. K. Hall and J. Genzer, *J. Chem. Phys.*, 2007, **127**, 144912.

59 A. B. Ozel, O. Srivannavit, J. M. Rouillard and E. Gulari, *Biotechnol. Prog.*, 2012, **28**, 556–566.

60 H. Binder, *J. Phys.: Condens. Matter*, 2006, **18**, S491–S523.

61 T. Ohzono, K. Katoh and N. Uchida, *Soft Matter*, 2025, **21**, 1233–1240.

62 G. Lee, B. Kim and D. K. Yoon, *Macromol. Rapid Commun.*, 2025, **46**, 2401086.

63 E. K. Hobbie, H. Wang, H. Kim, S. Lin-Gibson and E. A. Grulke, *Phys. Fluids*, 2003, **15**, 1196–1202.